*lubricants*

MDPI

*Article*

# Nanocomposite of Poly(L-Lactic Acid) with Inorganic Nanotubes of $WS_2$

**Hila Shalom [1], XiaoMeng Sui [1], Olga Elianov [1], Vlad Brumfeld [2], Rita Rosentsveig [1], Iddo Pinkas [2], Yishay Feldman [2], Nir Kampf [1], H.D. Wagner [1], Noa Lachman [3] and Reshef Tenne [1,*]**

1 Department of Materials and Interfaces, Weizmann Institute, Rehovot 76100, Israel; hila.shalom@weizmann.ac.il (H.S.); xiaomeng.sui@weizmann.ac.il (X.S.); olga.elianov@weizmann.ac.il (O.E.); rita.rosentsveig@weizmann.ac.il (R.R.); nir.kampf@weizmann.ac.il (N.K.); daniel.wagner@weizmann.ac.il (H.D.W.)

2 Department of Chemical Research Support, Weizmann Institute, Rehovot 76100, Israel; vlad.brumfeld@weizmann.ac.il (V.B.); iddo.pinkas@weizmann.ac.il (I.P.); Isai.Feldman@weizmann.ac.il (Y.F.)

3 Department of Materials Science and Engineering, Faculty of Engineering, Tel-Aviv University, Ramat Aviv, Tel Aviv 6997801, Israel; Noala@tauex.tau.ac.il

* Correspondence: reshef.tenne@weizmann.ac.il; Tel.: +972-8-9342-394

Received: 21 February 2019; Accepted: 20 March 2019; Published: 25 March 2019


**Abstract:** Composites of poly(L-lactic acid) (PLLA) reinforced by adding inorganic nanotubes of tungsten disulfide (INT–$WS_2$) were prepared by solvent casting. In addition to the pristine nanotubes, PLLA nanocomposites containing surface modified nanotubes were studied as well. Several surface-active agents, including polyethylene imine (PEI), were studied in this context. In addition, other biocompatible polymers, like poly D,L-lactic acid (PDLLA) and others were considered in combination with the INT–$WS_2$. The nanotubes were added to the polymer in different proportions up to 3 wt %. The dispersion of the nanotubes in the nanocomposites were analyzed by several techniques, including X-ray tomography microscopy (Micro-XCT). Moreover, high-temperature rheological measurements of the molten polymer were conducted. In contrast to other nanoparticles, which lead to a considerable increase of the viscosity of the molten polymer, the $WS_2$ nanotubes did not affect the viscosity significantly. They did not affect the complex viscosity of the molten PLLA phase, either. The mechanical and tribological properties of the nanocomposites were found to improve considerably by adding the nanotubes. A direct correlation was observed between the dispersion of the nanotubes in the polymer matrix and its mechanical properties.

**Keywords:** PLLA; solid lubricants; inorganic nanotubes

## 1. Introduction

Poly(lactic acid) (PLA) is a compostable thermoplastic derived from renewable plant sources, such as starch and sugar. Since lactic acid is a chiral molecule, PLA exists in three forms—L-PLA (PLLA), D-PLA (PDLA), and a racemic mixture of D,L-PLA (PDLLA) [1]. They all are biodegradable, compostable, and nontoxic to the human body and the environment. PDLLA is an amorphous polymer with degradation time of about a year for total absorption in the body, therefore it is usually considered for applications, such as drug delivery. On the other hand, PLLA is a semi-crystalline material with degradation time of longer than 5 years [2–7]. Therefore, PLLA is preferred in applications where high mechanical strength and toughness are required, like orthopedic prostheses. PDLLA is a random copolymer, consisting of L-lactic acid and D-lactic acid monomers; it is amorphous and cannot exhibit crystalline structures. Those polymers present lower strength and modulus compared

with polyglycolic acid (PGA) [8,9]. One of the biggest disadvantages of PLA (PLLA, PDLLA) is its low fracture toughness [10]. Meanwhile, it is known that addition of small amounts of nanofillers to the polymer matrix can enhance its mechanical properties, significantly compared with the neat polymer [11–17]. Various nanoparticles were considered as reinforcement to biodegradable polymers, including multi-walled carbon nanotube (MWCNT) [18–22], cellulose nanofiber (CNF) [23,24], and $TiO_2$ [25,26].

Inorganic nanotubes (INT) and fullerene-like (IF) nanoparticles of layered metal dichalcogenides $MX_2$ (M = transition metal, Mo, W, etc.; X = S, Se, Te) were first reported in 1992. Each transition metal (M) atom within the $MX_2$ layers, is covalently bonded to six chalcogen (X) atoms in trigonal prismatic coordination [27]. The $MX_2$ layers are stacked together via weak van der Waals forces. The multiwall INT nanostructures are 1–20 μm long with diameter of 30–150 nm (aspect ratio of 100 and larger). They exhibit very good mechanical properties. For instance, the Young's modulus of INT–$WS_2$ is around 150–170 GPa, bending modulus of 217 GPa, tensile strength between 16–22 GPa, and their strain $\varepsilon > 10\%$ [28,29]. Their favorable mechanical properties were attributed to the high degree of crystallinity of the multiwall nanotubes, obtained through high temperature chemical synthesis. In addition, the INT–$WS_2$ are chemically stable up to a temperature close to 350 °C in an oxidizing atmosphere and beyond 1000 °C in a reducing or neutral atmosphere. INT–$WS_2$ can be readily dispersed in organic solvents, polymers, epoxy resins, etc. Incorporating the nanotubes (0.1–2 wt %) into different polymers and inorganic phases, was shown to improve the mechanical and thermal behavior of different nanocomposites [30,31].

Furthermore, the addition of the nanotubes to different gels [32,33] and polymer matrices [34] in small amounts leads to a precipitous reduction in the friction forces, which may have important ramifications on numerous medical and other technologies. Equally important is the fact that several studies have indicated that IF/INT of $WS_2$ ($MoS_2$) are non-toxic and biocompatible [34–38]. One of the challenges in nanocomposites is the compatibility between the polymer matrix and the nanofillers, which entails that the interfacial interaction between the surfaces of the two phases cannot be easily tuned and matched. This fact suggests that suitable surface modifications of the nanotubes can produce a more intimate and stronger nanotube-polymer interactions. There are several reports on the functionalization of nanoparticles in the literature, using N-Methyl-2-pyrrolidone (NMP) [39–42], polyethylenimine (PEI) [43,44], polyethylene glycol (PEG) [45–49], and more. NMP, PEI, and PEG are well-known dispersants for nanoparticles in various matrices [43,50]. Biocompatibility is a prime concern in this case since otherwise the nanocomposite may not be suitable for biomedical applications. Several reports on the effect of nanotubes and fullerene-like nanoparticles of $WS_2$ incorporated in biodegradable/biocompatible polymers such as PLLA [51], poly(3-hydroxybutyrate) (PHB) [52], Poly(3-Hydroxybutyrate-co-3-hydroxyvalerate) (PHVB) [53], and others have appeared. These studies focused on the crystallization process of these thermoplastic polymers. They concluded that the addition of IF/INT induces a sharp rise in the nucleation rate and density of the polymer crystallites, which presumably leads to a reinforcement effect of the polymer matrix.

The INT–$WS_2$ and also other inorganic particles, like IF–$MoS_2$, INT–$MoS_2$, and IF–$WS_2$ confer excellent tribological properties when added in small amounts to a variety of lubricating fluids, offering them numerous applications [54–56]. The mechanisms involved in the tribological action of these nanoparticles have been investigated by a number of researchers, most notably via in situ transmission electron microscopy (TEM), scanning electron microscopy (SEM) [57], surface force apparatus (SFA) [58], and atomic force microscopy (AFM) [59]. Most notably, rolling, sliding, exfoliation, and also mending [60] were found to have paramount importance in explaining their superior tribological action.

This work also focuses on the influence of INT–$WS_2$ on the PLLA matrix using various techniques—the relationship between the mechanical properties of the nanocomposites' and the distribution of the nanotubes in the polymer matrix were evaluated by SEM, X-ray diffraction (XRD), differential scanning calorimetry (DSC), and X-ray tomographic microscopy (Micro XCT).

The friction of the polymer films with and without the nanotubes was measured using two different setups. These measurements indicated substantial reduction in the friction force for the polymer films containing minute amounts of the nanotubes. The rheological properties of the neat PLLA and the nanocomposites were measured at elevated temperatures. In contrast with other nanoparticle fillers, the addition of the nanotubes did not influence the polymer viscosity and the dynamic rheological parameters.

## 2. Experimental

### *2.1. Preparation of PLLA/PLLA–INT–$WS_2$ Nanocomposites*

Two types of PLLA, with an inherent viscosity midpoint of 2.4 and 3.8 dL/g purchased from Corbion (Gorinchem, The Netherlands), trade names: PLLA 24 and PLLA 38, were used in this study. Reference samples were prepared by dissolving 1 g of PLLA in 20 ml dichloromethane (DCM) (5 *w*/*v* %), mechanical stirring (10 min), and solvent-casting in Teflon dishes. PLLA films with different wt % INT–$WS_2$ were prepared by first fully dissolving the 1 g PLLA in 15 ml DCM and mechanical stirring (10 min). Multiwall $WS_2$ nanotubes were prepared by reacting $WO_3$ powder with $H_2S$ gas at elevated temperatures (850 °C) under a reducing atmosphere [61]. The diameter of the nanotubes varied between 40–150 nm and their length varied between 1–20 micrometer. Secondly, the nanotubes were fully dispersed in the rest of the DCM (5 ml) by ultrasonic bath treatment (about 5 min) and finally the two solutions were mixed together and mechanically stirred before solvent-casting in Teflon plates. The Teflon plates were dried in room temperature overnight. Subsequently, the films were vacuum annealed at 30 °C for a week and their weight loss was monitored, daily.

### *2.2. Functionalization of the INT-$WS_2$*

Several surface-modifying agents were used to functionalize the nanotubes N-Methyl-2-pyrrolidone (NMP), Polyethylenimine (PEI), and Polyethylene glycol (PEG).

- PEI: INT–$WS_2$ powder was sonicated at room temperature in a mixture of INT–$WS_2$: 2% aqueous solution of PEI in a ratio of 2 mg: 1 mL for 10 min. Subsequently, the suspension was centrifuged at 6000 rpm for 15 min and washed with distilled water. Finally, the suspension was dried at 50 °C for 24 h. The PLLA 24 films were prepared according to the description in Section 2.1 but with chloroform as a solvent instead of DCM.
- NMP: INT–$WS_2$ powder was sonicated for 30 min in a mixture of INT–$WS_2$: NMP: distilled water in a ratio of 2 mg:1 mL:2 mL. Subsequently, the suspension was annealed for 6 h at 120 C. The PLLA 38 films were prepared according to the description in Section 2.1.
- PEG: INT–$WS_2$ solution was mixed at room temperature in a mixture of INT–$WS_2$:DCM:PEG distilled water in a ratio of 1 mg:1 mL: 1 mg:20 mL. Subsequently, the solution was treated in ultrasonic bath for 30 min followed by centrifugation at 6000 rpm for 5 min and washed with distilled water to eliminate the excess polymer. The PLLA 24 films were prepared according to the description in Section 2.1.

### *2.3. Characterization Techniques*

#### 2.3.1. High-Resolution Scanning Electron Microscopy (HRSEM)

The morphology and structure of PLLA/INT-$WS_2$ nanocomposite films were characterized by HRSEM (Ultra 55, Zeiss, Oberkochen, Germany). In order to analyze the nanotubes distribution in the polymer, a cross-section of the sample was prepared by immersing in liquid nitrogen for a few minutes and then breaking the fragile specimen. In order to avoid the sample charging during the analysis (uncoated specimen), the cross-section was examined under relatively low accelerating voltage (1–2 kV) and low current. Secondary electrons (SE) and backscattering electron (BSE) detectors were used for the analysis.

#### 2.3.2. Mechanical Properties

The mechanical properties of the films were measured by performing tensile tests, using Instron-5965 (Instron, Norwood, MA, USA) equipped with a 5 kN load-cell at room temperature and a stretching speed of 1 mm/min. The samples were cut into strips, 5 mm wide and 50 mm long. The gauge length of the tested strip was 30 mm. The sample thickness was measured using SEM by measuring the cross-section of each sample along the sample length before the test. Five specimens were tested for each type of sample, and the results were given as average values. The load and displacement were recorded by a dedicated software provided by the manufacturer (Bluehill3, Norwood, MA, USA).

#### 2.3.3. X-ray Tomographic Microscopy (Micro-XCT)

The dispersion of the nanotubes in the PLLA matrix was imaged with a Zeiss Xradia Micro XCT 400 (Zeiss X-ray Microscopy, Pleasanton, CA, USA), under working conditions of a relatively low source voltage (40 kV) and current (200 μA). Image processing and analysis were done with the Avizo software. The voxel size was 0.3 μm. The images were corrected for beam hardening.

#### 2.3.4. Differential Scanning Calorimetry (DSC)

Differential scanning calorimetry (DSC) was performed with a DSC 250 (TA Instuments, New Castle, DE, USA). Temperature and enthalpy calibrations were performed using indium. The weighted samples were about 5 mg. They were placed in an aluminum pan and measured against an empty pan as a reference. Measurements were carried out under 50 mL/min nitrogen flow rate according to the following protocol: First, heating from 30 to 200 °C and 3 min at 200 °C (in order to erase the thermal history). Then, cooling down to 30 °C, and, finally, a 2nd heating until 200 °C. All scans were performed at 10 C/min under 50 mL/min nitrogen flow rate. From the mid-point of the (heating scan) thermograms, the glass transition ($T_g$), cold crystallization ($T_{cc}$), and melting ($T_m$) temperatures were determined. The crystallization temperature ($T_g$) was determined from the cooling scan. The degree of crystallinity was calculated from the DSC curves in two ways:

$$X_c = \frac{(\Delta H_m - \Delta H_{cc})}{\Delta H_m^\circ} \times 100\% \quad (1)$$

for heating [60–63], and

$$(1 - \lambda) = \frac{\Delta H_c}{\Delta H_m^\circ} \quad (2)$$

for cooling [50,51].

$\Delta H_m$, $\Delta H_{cc}$ (heating), and $\Delta H_c$ (cooling) are the melting enthalpy, cold crystallization enthalpy, and crystallization enthalpy (J/g), respectively; $\Delta H_m^\circ$, is the heat of fusion for completely crystallized PLA (93 J/g).

#### 2.3.5. X-ray Diffraction

X-ray diffraction of the PLLA films was performed in order to determine the degree of crystallinity of each sample. The samples were scanned by X-ray powder diffraction (XRD) using TTRAX III (Rigaku, Tokyo, Japan) theta-theta diffractometer equipped with a rotating copper anode X-ray tube operating at 50 kV/200 mA. The samples were scanned in specular diffraction mode (θ/2θ scans) from 5° to 60° (2θ) with a step size of 0.02° and a scan rate of 0.5° per min.

#### 2.3.6. Rheological Characterization

Dynamic shear rheological characteristics of the PLLA polymer and PLLA reinforced with 0.5 wt % INT–$WS_2$ were determined by using a strain/stress-controlled rheometer (Thermo-Haake MARS III, Karlsruhe, Germany) equipped with a Peltier heating system and a temperature-control

unit (HAAKE Heat Exchanger A, Thermo Scientific, Karlsruhe, Germany). The measurements were carried out using a plate–plate configuration with a plate diameter of 20 mm and a gap of 0.05 mm. The sample was placed between the plate–plate geometry and the measurement was started after preheating to 185 ± 0.1 °C.

Before starting the frequency sweep tests, a stress sweep test was applied at a range between 1–10,000 Pa to determine the linear viscoelastic regime (LVR) of the sample. Then, the frequency sweep test was conducted for all samples using a dynamic oscillatory shear rheometer at a frequency range of 0.1–100 Hz at a constant shear stress (3000 Pa, in LVR) in the LVR and constant temperature (185 ± 0.1 °C). The complex viscosity, storage ($G'$), and loss ($G''$) moduli spectra for both PLLA compositions were evaluated. Each measurement was replicated three times. The dynamic mechanical spectra parameters of $G'$ (storage modulus) and $G''$ (loss modulus) were calculated using the following equations [62]:

$$G' = G \times \cos\delta \quad (3)$$

$$G'' = G \times \sin\delta \quad (4)$$

where δ is the phase lag between stress and strain and $G$ is the shear modulus.

The complex viscosity η* can be calculated as

$$\eta^* = G^*/\omega \quad (5)$$

where ω is the angular frequency and the complex modulus is defined as $G^* = G' + iG''$ with $i = (-1)^{0.5}$.

#### 2.3.7. Friction Coefficient

The friction forces were measured by Instron 5965, using a standard fixture (2810-005). The measurements of the static and kinetic friction coefficient of films were carried out according to the ASTM D1894 standard. The measurements were performed by recording the load of a moveable sled with weight of 1.15 kg (speed of 150 mm/min) across a horizontal table. Pieces of 2 × 3 $cm^2$ were cut and glued to the lower surface of the sled. The static friction coefficient was derived from the peak of the first maximum (force) on the load curve. The kinetic friction coefficient was obtained by averaging the force between two pre-defined points along the track. The friction coefficient was defined as the recorded force divided by the mass of the sled (no extra load was applied). All the tests were performed at room temperature in air.

Three different measurements were carried out:

- PLLA 24 film and PLLA 24 film with 0.5 wt % INT–$WS_2$ were run 20 times on the steel table (the first 16 times served for running-in). The results of the last 4 measurements are reported.
- PLLA 24 film and PLLA 24 + 0.5 wt % INT–$WS_2$ film was rubbed 5 times on a silicon–carbide (SiC) paper (1200 grit) and then measured 3 times using the steel table.
- PLLA 24 film and PLLA 24 + 0.5 wt % INT–$WS_2$ film was rubbed 5 times on a SiC paper (150 grit) and then measured 3 times using the steel table.

#### 2.3.8. Friction Force

The friction force was measured using a modified fixture attached to the Instron 5965. The original fixture was described in a great detail elsewhere [31,32]. Here, a stainless-steel rod was moved in the bore of a soft polymer ring made of room temperature vulcanizing (RTV) silicone (vide infra). The stainless-steel rod with cylindrical shape (8 mm dimeter) was fixed to the lead with two screws and attached to the load cell of the Instron. The lead was inserted into the RTV silicone ring in the model and the retraction force was measured while extracting the metallic lead from the ring at a speed of 50 mm/min. In every set of measurements, three different stainless-steel rods were used: Clean rod, rod coated by dip coating in the neat polymer solution, and in polymer solution containing 0.5 wt % INT–$WS_2$ as described in Section 2.1. Different types of polymer films were used for coating

the rod. They were: PLLA 24, PLLA 38, PLLA with a viscosity of 2.1 dL/g (RESOMER L210), PDLLA (viscosity of 0.55 dL/g, Lakeshore Biomaterials), and PDLGA 50/50 (viscosity of 0.4 dL/g, Lakeshore Biomaterials, Birmingham, AL, USA). The values of the polymer viscosities were provided by the supplier. The viscosity of the polymers was measured (by the supplier) in $CHCl_3$ at 25 °C or 30 °C. No run-in procedure was undertaken in this study for the different samples.

#### 2.3.9. Raman Spectroscopy

Raman spectra of the films were obtained with a Horiba-Jobin Yivon (Lille, France) LabRAM HR Evolution setup using solid-state laser with a wavelength of 532 nm. The instrument was equipped with an Olympus objective MPlan N 100× NA 0.9. The measurements were conducted using a 600 grooves/mm grating. Each spectrum was acquired for 20 s and the spectra were averaged 2 times, which enabled using low excitation power (about 1 mW) thereby preserving the sample integrity. The spectral ranges collected were from 70 to 3400 $cm^{-1}$. In addition, Raman mapping was performed on the cross section of PLLA film with 0.5 wt % INT–$WS_2$. An area of (5 × 5 $\mu m^2$) of the cross-section was scanned during these measurements.

## 3. Results and Discussion

The weight loss of the polymer films during the drying process, i.e., heating at 30 °C under vacuum, is reported in Figure S1. A significant weight loss occurred in the first day of the drying and, subsequently, more gradual weight loss was observed for the film. The addition of the nanotubes to the polymer did not have a marked effect of the solvent evaporation. The morphology of the cross-section of the neat PLLA film and with different concentrations of INT–$WS_2$ was examined by HRSEM. This analysis showed that the nanotubes were successfully embedded in the polymer and they were very well dispersed in the polymer matrix; see Figure 1A,B for PLLA 24 and PLLA 38, respectively (the nanotubes are circled in red color for facile tracking). The specimens were prepared by immersion in liquid nitrogen and breaking. The morphology of the specimens was studied by low-voltage SEM in order to prevent charging due to the low electrical conductivity of PLLA. The morphology of the two specimens were quite different. While the PLLA 24 presented a relatively smooth surface, the surface of the broken PLLA 38 was rather rough. The surface of the PLLA 38 was quite rough due likely to its low fracture toughness and brittleness. The nanotubes were positioned between the fractured planes, which is a common behavior of nanotubes as nanofillers in reinforced polymer matrices and, hence, contribute to the polymer reinforcement.

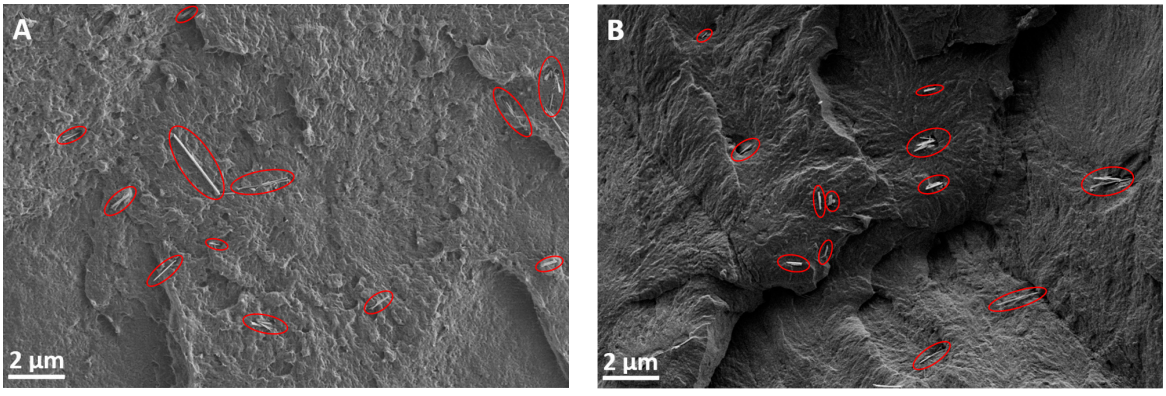


**Figure 1.** High-resolution scanning electron microscopy (HRSEM) images of the cross-section: (**A**) poly(L-lactic acid) (PLLA) 24 with 0.5 wt % inorganic nanotube (INT)–$WS_2$ film, (**B**) PLLA 38 with 0.5 wt % INT–$WS_2$ film; the $WS_2$ nanotubes are encircled by red color.

The mechanical properties of PLLA 38 and PLLA 24 films are summarized in Table 1; Table 2, respectively, and their stress–strain curves are presented in Figure 2. The modulus and the strength

of the PLLA 38 films was considerably improved as the nanotube concentrations increased. On the other hand, the elongation and toughness (area under the stress–strain curve) showed the largest improvement around 0.5 wt % INT (the same as for carbon nanotubes). In addition, the modulus and the strength of PLLA 24 films exhibited the largest improvement around 0.5 wt % nanotubes, but the elongation and toughness increased as the concentration of nanotubes increased to 0.8 wt %.

**Table 1.** Mechanical properties of PLLA 38 films.

| Sample | Modulus (GPa) | Yield Strength (MPa) | Elongation (%) | Toughness (MPa*%) | Thickness (mm) |
|---|---|---|---|---|---|
| PLLA 38 film | 1.6 ± 0.1 | 26.6 ± 1.5 | 3.2 ± 0.4 | 0.6 ± 0.1 | 0.15 ± 0.1 |
| PLLA 38 film with 0.25 wt % INT–$WS_2$ | 1.8 ± 0.02 | 29.7 ± 1.2 | 2.9 ± 0.3 | 0.6 ± 0.1 | 0.12 ± 0.1 |
| PLLA 38 film with 0.4 wt % INT–$WS_2$ | 1.9 ± 0.1 | 39.5 ± 2.0 | 5.4 ± 0.7 | 1.5 ± 0.2 | 0.11 ± 0.1 |
| PLLA 38 film with 0.7 wt % INT–$WS_2$ | 2.4 ± 0.1 | 46.1 ± 1.5 | 3.7 ± 0.5 | 1.1 ± 0.2 | 0.10 ± 0.1 |

**Table 2.** Mechanical properties of PLLA 24 films.

| Sample | Modulus (GPa) | Yield Strength (MPa) | Elongation (%) | Toughness (MPa*%) | Thickness (mm) |
|---|---|---|---|---|---|
| PLLA 24 film | 1.4 ± 0.05 | 22.0 ± 4.1 | 3.5 ± 0.6 | 1.2 ± 0.3 | 0.14 ± 0.1 |
| PLLA 24 film with 0.25 wt % INT–$WS_2$ | 1.8 ± 0.05 | 41.5 ± 1.4 | 8.1 ± 1.5 | 2.0 ± 0.4 | 0.11 ± 0.1 |
| PLLA 24 film with 0.5 wt % INT–$WS_2$ | 2.8 ± 0.2 | 60.9 ± 2.8 | 18.4 ± 5.2 | 5.7 ± 0.7 | 0.10 ± 0.1 |
| PLLA 24 film with 0.8 wt % INT–$WS_2$ | 2.2 ± 0.2 | 43.7 ± 3.5 | 10.3 ± 2.4 | 3.8 ± 1.2 | 0.10 ± 0.1 |

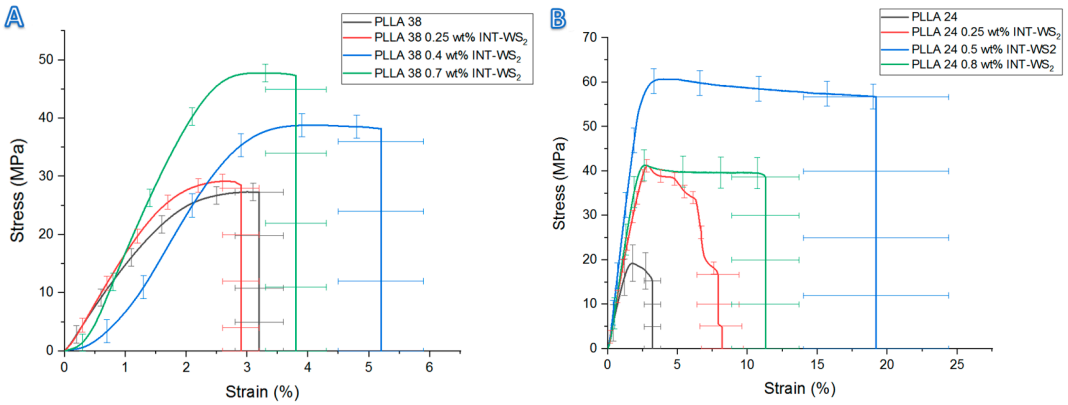


**Figure 2.** Stress–strain curves of PLLA 38 (**A**) and PLLA 24 (**B**) films with different weight percentage of INT–$WS_2$ with error bars. The results for each specimen represent an average value of five samples.

### *3.1. X-ray Tomographic Microscopy (Micro-XCT)*

Micro-XCT analysis was performed for PLLA films with different concentrations of the nanotubes. The goal of this analysis was to understand the relationship between the dispersion of the nanotubes in the polymer matrix and the mechanical function of the nanocomposite. Alternatively, the distribution of carbon nanotubes in hydroxyapatite bioceramics was studied by 3D-microstructure reconstruction following serial sectioning and analysis [63]. Obviously, the latter method can provide more detailed microscopic information on the specimen, but is rather tedious and time consuming. The resolution of the current micro-XCT is limited to about half a μm. Therefore, the precise number of nanotubes present in each white spot could not be determined. In fact, it was not possible to judge if individual nanotubes could be resolved at all. Agglomerates of the nanotubes, which are represented as large blocks of white area, could be, nonetheless, easily scrutinized. Table 3 shows the mechanical properties of the PLLA films which were also analyzed via the micro-XCT (note that dedicated specimen was prepared for this study and the mechanical properties were somewhat different from those reported in Tables 1 and 2 and for the same materials).

**Table 3.** Mechanical properties of PLLA films measured in micro-XCT analysis (the blank films are added for reference only).

| Number | Sample | Modulus (GPa) | Yield Strength (MPa) | Elongation (%) | Toughness (MPa*%) | Thickness (mm) |
|---|---|---|---|---|---|---|
| 1 | PLLA 38 film | 1.6 ± 0.1 | 26.6 ± 1.5 | 3.2 ± 0.4 | 0.6 ± 0.1 | 0.15 ± 0.1 |
| 2 | PLLA 38 film with 0.5 wt % INT–$WS_2$ | 2.4 | 49.3 | 14.0 | 6.1 | 0.14 |
| 3 | PLLA 38 film with 1 wt % INT–$WS_2$ | 4.0 | 68.25 | 29.8 | 20.0 | 0.11 |
| 4 | PLLA 38 film with 3 wt % INT–$WS_2$ | 3.4 | 57.4 | 11.7 | 4.9 | 0.13 |
| 5 | PLLA 24 film | 1.4 ± 0.05 | 22.0 ± 4.1 | 3.5 ± 0.6 | 1.2 ± 0.3 | 0.14 ± 0.1 |
| 6 | PLLA 24 film with 0.5 wt % INT–$WS_2$ | 2.4 | 60.7 | 75.7 | 40.5 | 0.12 |
| 7 | PLLA 24 film with 0.5 wt % INT–$WS_2$ | 2.0 | 40.7 | 3.2 | 1.0 | 0.13 |

PLLA 38 film with 0.5 wt % INT–$WS_2$ (sample 2 in Table 3 and Figure 3 and Figure S2) showed good dispersion of the nanotubes in the film with very little agglomeration, before and after the tensile test. In addition, comparing between the figures, one can notice the change in the orientation of the nanotubes due to the loading of the sample during the tensile test. For example, the surface area of the sample before the stretch was a combination of bright (nanotubes) and dark (polymer) areas (see Figure 3 and Figure S2). The bright area largely reflects the random orientation of the tubes. After the stretch, the surface area of the bright zones was reduced, especially in the middle of the sample in the head-on configuration. This effect is believed to be caused by to the alignment of the nanotubes along the loading direction, which reduces their cross-section with respect to the X-ray radiation. Note also that, due to partial precipitation of the tubes during the preparation of the film (via solvent evaporation), the bottom face (right surface at 270°) appears thicker than the top surface of the film (left).

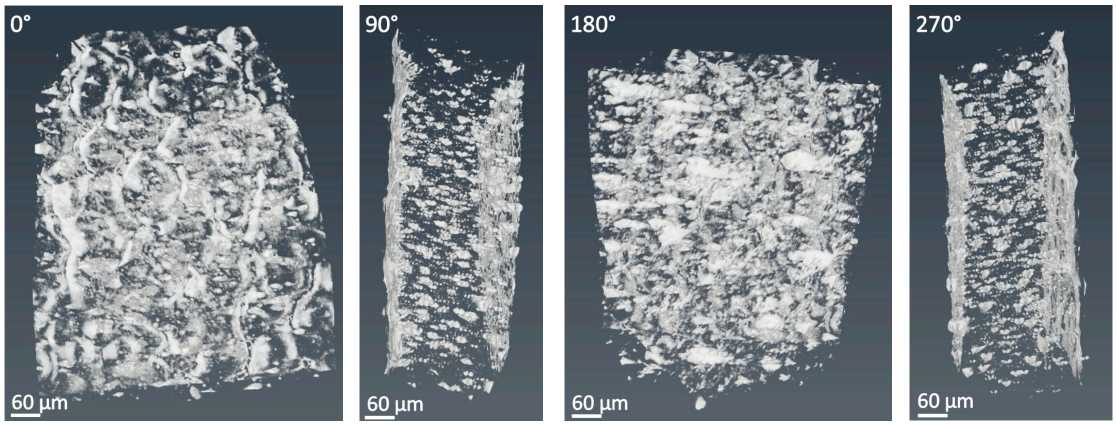


**Figure 3.** Images obtained by revolving the film in 360° (sample No. 2 in Table 3) obtained with micro-XCT before tensile test. Please note that the pictures are shown in 3D perspective. Consequently, the thickness of the surface layer enriched with nanotubes is largely exaggerated. However, the difference between the top (thin) and bottom (thick) layer enriched with agglomerated nanotubes is clearly visible.

In contrast to that, the PLLA 38 film with 1 wt % INT–$WS_2$ (sample No. 3 in Table 3) before and after tensile test (Figures S3 and S4) showed significant agglomeration of the nanotubes and sedimentation at the bottom of the samples. The sedimentation is clearly visible by the difference in contrast between the two sides of the samples in a head-on view. The bottom bright film (left side in the 270° view) is much thicker than the upper surface film (right side in 270°). The agglomeration-sedimentation is the result of the lengthy drying process, which is required in order to get rid of the solvent. Despite the presence of the nanotubes' agglomerates, this film showed improved mechanical properties (strength and ductility) compared with the neat PLLA and PLLA with 0.5 wt % INT–$WS_2$. This observation shows that the agglomeration of the nanotubes can lead to partial improvements in the mechanical properties by transferring the load from the polymer matrix to the nanotubes' agglomerates. However, it is

believed that better dispersion of the nanotubes would lead to further improvement of the mechanical properties of the 1 wt % nanotube sample fulfilling the full potential of the nanotubes to reinforce the polymer matrix.

PLLA 38 film with 3 wt % INT–$WS_2$ (sample No. 4, Table 3) before the tensile test (Figure S5) showed extensive agglomeration of the nanotubes and their sedimentation at the bottom of the film, near the surface of the Teflon plates used for the preparation of the specimen. The agglomeration in this sample explains the premature failure of the film in this concentration by reducing the ductility and toughness compared to the specimen with lower concentrations of the nanotubes. In addition, the surface of this sample was decorated by lines in the film at 180° projection (see Figure 4). These lines are believed to emanate from the inadequate polishing of the Teflon plates' surface. These trenches prevented transfer of the load from the polymer matrix to the nanotubes' agglomerates uniformly along the specimen.

Micro-XCT analysis was also performed on PLLA 24 films. This analysis was intended to compare the nanotubes distribution in the specimens exhibiting both very good and pretty bad mechanical properties. For instance, two samples were selected for this comparison and their mechanical properties are also reported in Table 3. First, the micro-XCT analysis showed a big improvement in the dispersion of the nanotubes in PLLA 24 (Figures 4–8) compared with PLLA 38 (Figure 3 and Figures S2–S5).

The Micro-XCT analysis of PLLA 24 films with 0.5 wt % INT–$WS_2$ with long extension (75%) before and after tensile test are shown in Figure 4; Figure 5. Indeed, the nanotubes exhibited a very good dispersion in the film with a smooth surface and homogeneous thickness. The even distribution of the nanotubes prevented weak links, which helped the sample to achieve longer extension by dividing the load uniformly along its entire length.

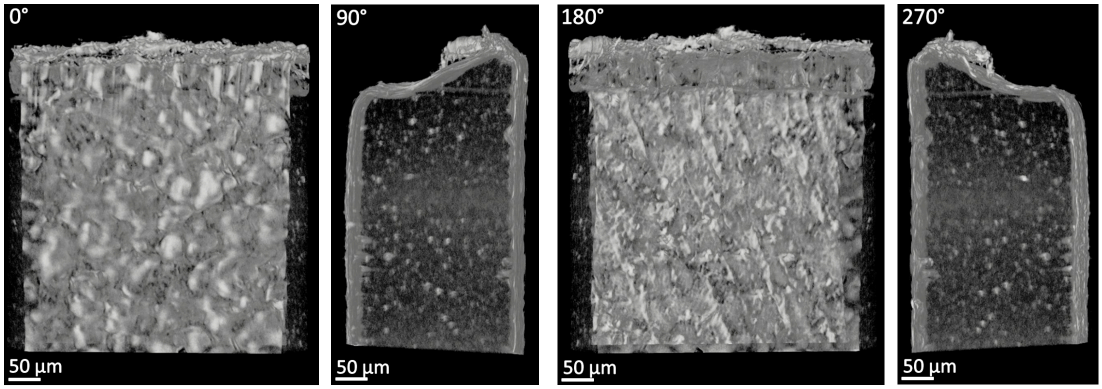


**Figure 4.** Images from the 360° projection obtained with the micro-XCT of PLLA 24 film with 0.5 wt % INT–$WS_2$ (sample No. 6 in Table 3). This sample exhibited a long extension (75%), the reported analysis was done before the tensile test. The stripes visible in 180° projection were the result of the surface modulation of the Teflon container used for the preparation of the specimen.

In contrast to that, the results for PLLA 24 film with 0.5 wt % INT–$WS_2$ (No. 7) with short extension (3.2%) before and after tensile test are shown in Figure 6; Figure 7. The agglomeration of nanotubes led to their partial precipitation during the drying of the specimen and their sedimentation at the bottom of the film, which resulted in a rough surface and homogeneous thickness and can be clearly observed in 90° and 270° in Figure 7. The appearance of protrusions at the surface made it highly non-uniform and produced weak links and poor mechanical behavior for this specimen. The Micro-XCT analysis can also show the cross-section across the sample in all three planes. From this analysis (Figure 8), the bulges at the surface appeared to be placed above a nanotubes' agglomerate which precipitated at the bottom of the sample. Therefore, the nanotubes' agglomerate was a failure point (weak link) in the matrix, which prevented uniform evaporation of the solvent, and eventually caused roughening of the surface.

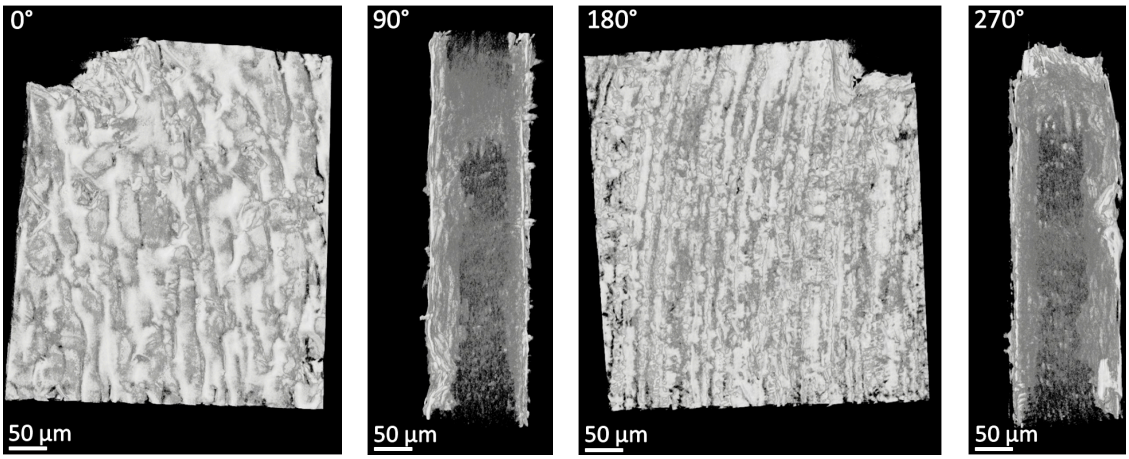


**Figure 5.** Images from the 360° video in the micro-XCT of PLLA 24 film with 0.5 wt % INT–$WS_2$ (sample No. 6 in Table 3) with long extension after the tensile test. Shear bands of the strained sample are clearly visible at 0° and 180°. The thickness of the strained sample visible at 90° and 270° are appreciably smaller than those in Figure 4 (before straining).

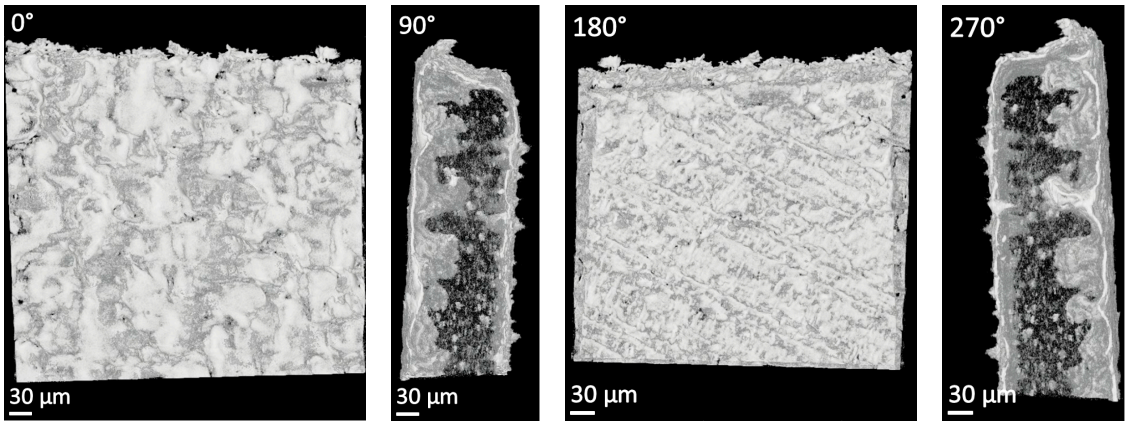


**Figure 6.** Images from the 360° video in the micro-XCT of PLLA 24 film with 0.5 wt % INT-$WS_2$ (sample No. 7 in Table 3) with short extension before the tensile test. The stripes visible in 0° are obtained by the surface modulation of the Teflon container used for the preparation of the specimen.

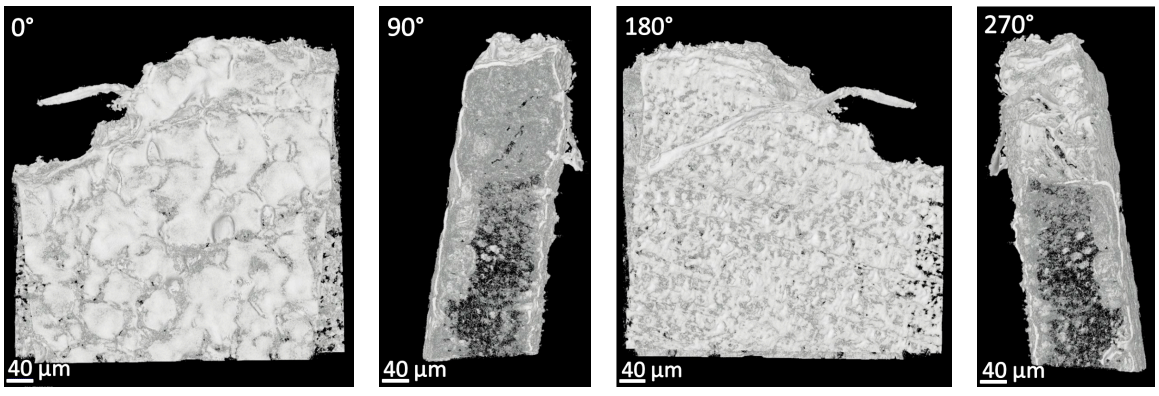


**Figure 7.** Images from the 360° video in the micro-XCT of PLLA 24 film with 0.5 wt % INT–$WS_2$ (sample No. 7 in Table 3) with short extension after the tensile test. The stripes visible in 0° are obtained by the surface modulation of the Teflon container used for the preparation of the specimen.

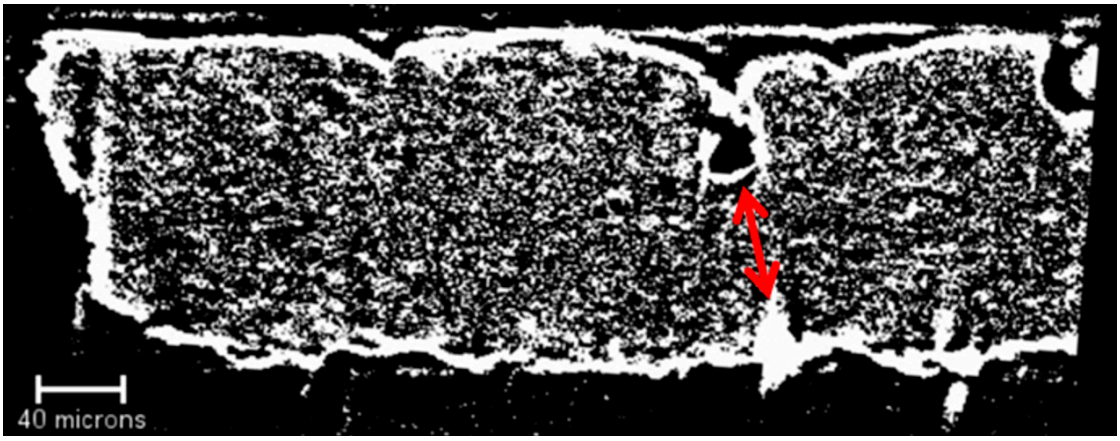


**Figure 8.** Images from the YZ slicing of the micro-XCT video of PLLA 24 film with 0.5 wt % INT–$WS_2$ (No. 7 in Table 3) with short extension before the tensile test. The white contrast is produced by the X-ray absorption of the nanotubes in the PLLA polymer.

### *3.2. Functionalization of the INT-$WS_2$*

Occasionally, SEM analysis of the cross-section of the PLLA matrix with nanotubes dispersed therein, after breaking the specimen in liquid nitrogen, were carried out. As shown in Figure 9, circles around the nanotubes were observed, representing breaking points. This phenomenon indicates the relatively poor adhesive forces between the nanotubes and the polymers. These observations suggested that functionalization of the nanotubes surface could be useful for enhancing their binding to the polymer matrix.

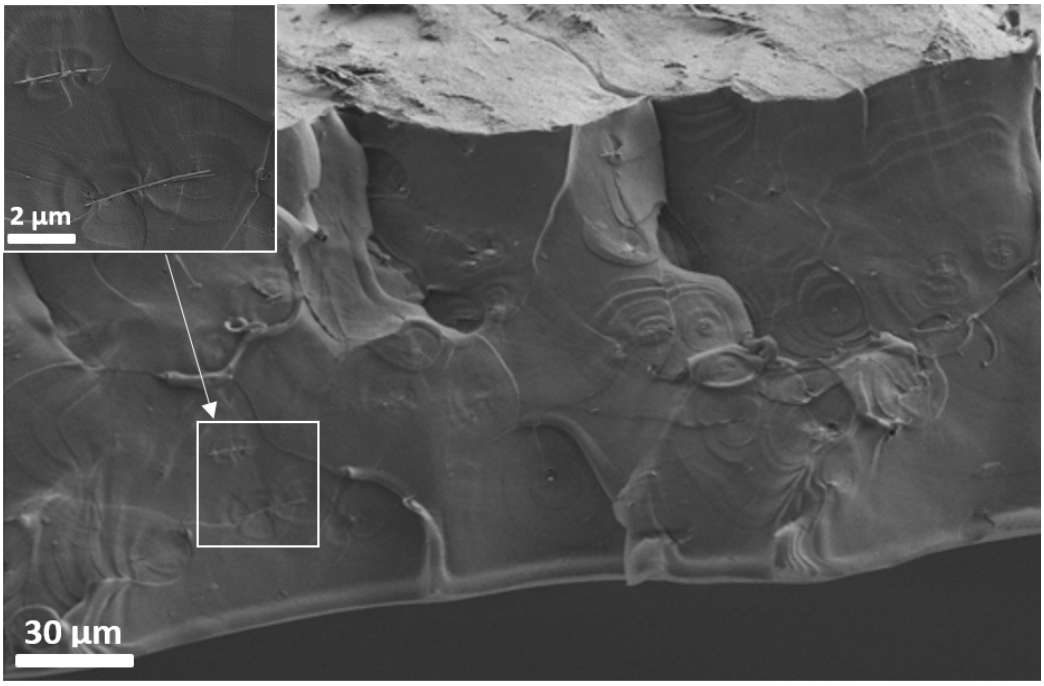


**Figure 9.** SEM image of the cross-section of PLLA 24 film with 0.5 wt % INT–$WS_2$ after breaking of the specimen immersed in liquid nitrogen.

Functionalization of INT–$WS_2$ with PEI (Polyethylenimine)

The PEI-treated nanotubes could not be dispersed in the solvent (DCM). Hence, this solvent was replaced by chloroform in these experiments. Fortunately, the PEI dissolves in chloroform very well making it suitable for the present experiments. Table 4 shows the mechanical properties of

a PLLA 24 film reinforced by neat and PEI-treated nanotubes. The blank samples showed high values of elongation, which indicated that the chloroform solvent was not fully evaporated from the matrix. This result should be compared to the DCM solvent, which was fully evaporated from the polymer matrix after one week of vacuum annealing (see Figure S1). The PLLA 24 compounded with untreated nanotubes exhibited slight improvements in the mechanical properties compared with the neat polymer. The PEI-treated nanotubes showed further improvements in the mechanical properties, especially around 0.5 wt % INT–$WS_2$ (up to 165% improvement compared with neat nanotubes). Therefore, one can conclude that the PEI functionalization increased the polymer-nanotubes interfacial interaction. However, no improvement was recorded for the 0.25 wt % INT–$WS_2$ compared to the blank polymer. This observation entails that the functionalization of the nanotubes with PEI did not contribute much to the adhesion between the PEI-treated nanotubes in low weight percentage.

**Table 4.** Mechanical properties of PLLA 24 film (solvent: chloroform) with neat nanotubes and PEI-treated nanotubes.

| Sample | Modulus (GPa) | Yield Strength (MPa) | Elongation (%) | Toughness (MPa*%) | Thickness (mm) |
|---|---|---|---|---|---|
| PLLA 24 film | 1.2 ± 0.1 | 22.0 ± 1.7 | 14.9 ± 6.7 | 1.5 ± 0.7 | 0.14 ± 0.1 |
| PLLA 24 film with 0.5 wt % INT–$WS_2$ | 1.6 ± 0.1 | 31.5 ± 0.7 | 9.2 ± 1.4 | 2.3 ± 0.4 | 0.1 ± 0.1 |
| PLLA 24 film | 2.1 ± 0.3 | 39.0 ± 3.0 | 26.6 ± 6.2 | 9.2 ± 2.2 | 0.12 ± 0.1 |
| PLLA 24 film with 0.25 wt % INT–$WS_2$ after functionalized with PEI | 1.2 ± 0.1 | 24.6 ± 3.0 | 58.3 ± 44.2 | 14.0 ± 12.0 | 0.14 ± 0.1 |
| PLLA 24 film with 0.5 wt % INT–$WS_2$ after functionalized with PEI | 2.65 ± 0.2 | 47.3 ± 3.8 | 41.5 ± 29.5 | 16.3 ± 13.5 | 0.09 ± 0.1 |
| PLLA 24 film with 1 wt % INT–$WS_2$ after functionalized with PEI | 2.15 ± 0.2 | 39.4 ± 1.9 | 15.1 ± 16.6 | 4.4 ± 5.35 | 0.1 ± 0.1 |

Further experiments with nanotubes functionalized with NMP (n-methyl-2-pyrrolidone) and PEG (polyethylene glycol) are described in the Supplementary Materials sections S3.2.2 and S3.2.3, Table S1, Table S2 and Figure S6.

### *3.3. Differential Scanning Calorimetry (DSC)*

The $T_g$, $T_{cc}$, $T_m$ $\Delta H_{cc}$, and $\Delta H_m$ were calculated from the DSC heating curves (see Supplementary Materials Figure S7). $T_c$ and $\Delta H_c$ were obtained from the cooling curves.

Table 5 shows the degree of crystallinity as well as the glass transition temperature of pristine PLLA 24 films and films with 0.5 wt % INT–$WS_2$ immediately after preparation and after a year. The neat PLLA 24 presented a very low degree of crystallinity (1.6% heating; 2.1% cooling), which could be attributed to the preparation processing, i.e., solvent casting and vacuum annealing at 30 °C. The low value of crystallinity remained virtually unchanged after one year. In contrast, the PLLA 24 film containing 0.5 wt % INT–$WS_2$ presented a relatively high value of crystallinity (37.4% heating and 32.9% cooling). After one year, the specimen with the nanotubes showed a ~20% drop in crystallinity. It can be concluded, therefore, that the nanotubes function as a promoter for nucleation and crystallization in the polymer matrix [50]. In addition, the crystallinity suffers mild depreciation after a delay of one year (~20%), which entail that the nanotubes function also as inhibitor for the PLLA degradation.

**Table 5.** DSC parameters of PLLA 24 and PLLA with 0.5 wt % INT–$WS_2$ films. (**A**) immediately after preparation and (**B**) after one year.

| | Sample | $T_g$ (°C) | $T_{cc}$ (°C) | $\Delta H_{cc}$ (J/g) | $T_m$ (°C) | $\Delta H_m$ (J/g) | $T_c$ (°C) | $\Delta H_c$ (J/g) | $X_c$ (%) | $(1-\lambda)_c$ (%) |
|---|---|---|---|---|---|---|---|---|---|---|
| A | PLLA 24 | 61.7 ± 0.4 | 114.8 ± 0.3 | 32.4 ± 12.0 | 178.6 ± 0.4 | 33.9 ± 12.2 | 101.6 ± 0.4 | 2.0 ± 0.1 | 1.6 ± 0.2 | 2.1 ± 0.4 |
| | PLLA 24 with 0.5 wt % INT-$WS_2$ | 65.5 ± 1.7 | 107.9 ± 7.9 | 3.1 ± 0.6 | 178.9 ± 0.3 | 37.9 ± 1.5 | 103.0 ± 0.9 | 30.6 ± 6.1 | 37.4 ± 2.1 | 32.9 ± 6.6 |
| B | PLLA 24 | 61.8 ± 0.3 | 114.6 ± 0.6 | 38.9 ± 3.4 | 178.8 ± 0.5 | 39.2 ± 3.4 | 101.8 ± 0.2 | 2.2 ± 0.4 | 0.3 ± 0.01 | 2.4 ± 0.4 |
| | PLLA 24 with 0.5 wt % INT-$WS_2$ | 62.2 ± 0.2 | 100.4 ± 0.8 | 6.7 ± 2.2 | 178.8 ± 0.4 | 35.4 ± 0.8 | 100.3 ± 0.2 | 23.9 ± 1.2 | 30.9 ± 2.5 | 25.6 ± 1.3 |

### *3.4. X-ray Diffraction*

XRD analysis of PLLA 38 is shown in Figure S8A–C for three specimens, respectively: Film of the neat polymer (blank), film with 1 wt % INT–$WS_2$, and PLLA 38 wires with 1 wt % INT–$WS_2$. Samples A and B were prepared by solvent casting and sample C was produced by extrusion. The XRD patterns of the samples B and C show an additional (002) peak of $WS_2$ nanotubes at about 14.4 degrees. One can conclude that, the crystallinity of the polymer was not influenced by the addition of the nanotubes, verified by comparing Sample A (neat polymer) and sample B (polymer with the nanotubes). Not surprisingly, the extruded wire (sample C) showed the highest and the narrowest FWHM of the 16.5° PLLA peak, and negligible intensity for the other PLLA peaks [64]. This observation suggests that the polymer in the extruded wire has a preferred orientation. Due to the texture in sample C, it is not possible to compare its degree of crystallinity with the other samples (A and B). Figure S9 displays the XRD pattern of the two samples presented in Figure S8A,B but in a higher-resolution scanning mode. This result shows a decreasing intensity of the spectrum profile at angles between 5° and 25° for the sample with INT–$WS_2$ in comparison with the neat polymer (PLLA 38). This reduction is attributed to the lower irradiation volume (lower X-ray penetration depth) in the sample with INT–$WS_2$ (tungsten has much higher X-ray absorption coefficient than the light elements of the polymer). The degree of crystallinity of samples A and B was calculated by comparing the total area under all the crystal peaks and the area under the amorphous halo. This calculation shows that the crystallinity of the neat PLLA 38 was about 60%, while the PLLA 38 with 1 wt % INT–$WS_2$ had a crystallinity of about 70%. Thus, the nanotubes induced increased crystallinity of the polymer but the error range for the XRD of all the samples was too large to make a definite conclusion regarding the influence of the nanotubes on the PLLA crystallinity, an effect which has to be further studied in the future.

Another XRD analysis was performed with the neat PLLA 24 film and one with 0.5 wt % INT immediately after fabrication and one year later (kept in a desiccator). The black curve (Figure S10) shows the XRD pattern of the PLLA 24 specimen with nanotubes immediately after preparation. The same sample one year later was examined by XRD (blue and purple curves). The sample was exposed to the XRD radiation from both sides. It appears that the two faces of the specimen exhibited a similar XRD pattern for the PLLA 24 peaks (16.5°, 18°, and 22°) and did not vary compared with the sample analyzed immediately after fabrication (black curve). The blank sample (not shown) did not reveal any degradation in its crystallinity after one year in desiccator, either. One can therefore conclude that the PLLA 24 fabricated by casting a film from DCM is stable for at least one year under the vacuum conditions of the desiccator (blue and purple curves). Interestingly though, the two sides of the samples showed different signal, with the back surface (blue curve) showing higher intensity of the 14.4° signal than the front surface (purple curve). This result is consistent with the Micro-XCT analysis, which clearly showed partial sedimentation of the nanotubes during the evaporation of the solvent.

### *3.5. Rheological Characterization*

Rheological measurements were performed with neat PLLA and PLLA with 0.5 wt % INT–$WS_2$ samples in order to study the influence of the nanotubes on the polymer matrix. Figure 10 shows the variation of the storage ($G'$) and loss ($G''$) moduli and complex viscosity ($\eta^*$) vs. sweep frequency for the samples. The storage and the loss moduli increased as a function of the frequency, which indicate that the polymer chains are fully relaxed and the polymer is in its rubbery zone. The complex viscosity decreased as a function of the frequency showing typical non-Newtonian shear thinning viscosity [65] behavior in which the complex viscosity decreased linearly with logarithmic increase of the angular frequency. The addition of the nanotubes to the polymer matrix did not lead to significant changes in the results.

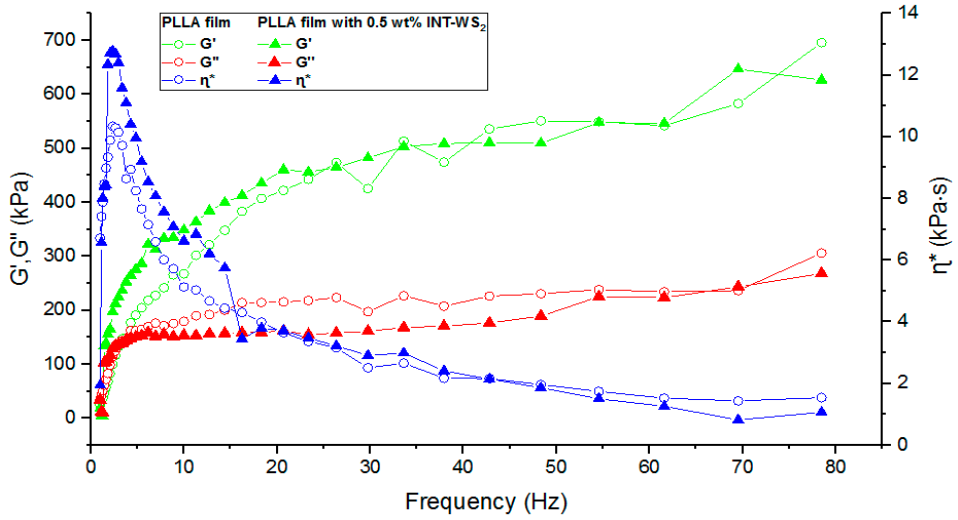


**Figure 10.** The complex viscosity (η*), the storage modulus ($G'$), and loss modulus ($G''$) vs. frequency for PLLA film and PLLA films with 0.5 wt % INT–$WS_2$ at 185 °C.

It is well accepted that addition of even small amounts of carbon nanotubes to polymers increases the static and the dynamic viscosities as well as the storage and loss moduli of the nanocomposite considerably [66,67]. Conversely, the $WS_2$ nanotubes exhibit little tendency to agglomerate and their influence on the rheological properties of the nanocomposites is very minor, if any. This effect can be attributed to the preferable lubricating behavior of these nanotubes, which also affect low drag on the nearby fluid molecules. These characteristics have important ramifications on the dispersion of the $WS_2$ nanotubes in the polymer matrix and the future manufacturing processes of such nanocomposites.

### *3.6. Friction Coefficient*

The cylindrical structure of INT–$WS_2$ (and the quasi-spherical structure of the fullerene-like $WS_2$ nanoparticles–IF–$WS_2$) suggested that they can roll under the combined action of shear and load. This hypothesis was confirmed through a long series of experiments [68]. Indeed, the IF nanoparticles are commercially used as superior solid lubricants for a variety of tribological applications and also for polymer reinforcement. However, measurements done with native PLLA samples containing the nanotubes (without any surface treatment or run-in procedure) did not show any improvement compared with the neat polymer samples. Running-in the sample 20 times back and forth, or rubbing the surface with SiC paper, had a major influence with precipitous reduction of the friction coefficient for samples containing the nanotubes as shown in Table 6.

**Table 6.** Friction coefficients of PLLA 24 films: $\mu_s$, static friction; $\mu_k$, kinetic friction.

| Type of Test | PLLA 24 Film | | PLLA 24 Film with 0.5wt % INT–$WS_2$ | |
|---|---|---|---|---|
| | $\mu_s$ | $\mu_k$ | $\mu_s$ | $\mu_k$ |
| Run 20 times on steel plate | 0.2 ± 0.01 | 0.19 ± 0.01 | 0.06 ± 0.01 | 0.03 ± 0.01 |
| After 5 (run-in) runs on 1200 SiC paper | 0.21 ± 0.01 | 0.18 ± 0.02 | 0.07 ± 0.05 | 0.03 ± 0.01 |
| After run 5 times on 150 SiC paper | 0.24 ± 0.02 | 0.21 ± 0.01 | 0.06 ± 0.01 | 0.03 ± 0.01 |

The static ($s$) and kinetic friction ($k$) of the PLLA 24 films show a major reduction in the friction of the films with the nanotubes compared to the blank (PLLA 24 film). The rubbing of the sample with SiC paper led to a wear and partial release of the nanotubes buried in the polymer matrix under the surface. Therefore, the rubbed specimen exhibited a larger reduction in the friction values compared to the samples run 20 times back and forth (run-in). Quantitatively, the static friction was reduced 3 times and the kinetic friction 7.5 times, compared with neat PLLA films for samples rubbed 5 times with SiC 150 grit. After running five times on 1200 SiC paper, the static friction was reduced 3.7 times and only 5.7 times for the kinetic friction.

### *3.7. Friction Force*

The normalized average traction force for uncoated and polymer coated stainless-steel (SS) rods were tested with a setup used previously as a mock-up for friction measurements of urological devices (UM model) [31,32] (Figure S11) and are summarized in Table 7. The coatings (of the SS rod) were prepared from different neat polymers and those containing 0.5 wt % INT–$WS_2$. Measurements were carried out in both dry and wet (water) conditions. The coatings of the rods were made by dip coatings. A very thin coating film (50–100 μm) was obtained, which allows one to see right away the tribological effects of the nanotubes impregnated in the thin polymer's coatings, without any run-in or rubbing procedure. Friction measurements in wet (water) conditions were measured to simulate more closely in vivo tests.

**Table 7.** Normalized traction force of the lead from the urethra model (UM) [31,32] with different polymers. Blank—polymer without nanotubes. Each number in the table represents an average of three measurements in dry and wet conditions.

| Sample | PLLA 38 | | PLLA 24 | | PLLA (2.1 dL/g) | | PDLLA (0.55 dL/g) | | PDLGA 50/50 (0.4 dL/g) | |
|---|---|---|---|---|---|---|---|---|---|---|
| | Dry | Wet | Dry | Wet | Dry | Wet | Dry | Wet | Dry | Wet |
| SS rod | 1.00 | 1.00 | 1.00 | 1.00 | 1.00 | 1.00 | 1.00 | 1.00 | 1.00 | 1.00 |
| Blank | 1.73 | 1.73 | 1.75 | 2.66 | 1.42 | 1.41 | 1.57 | 1.38 | 1.47 | 1.30 |
| 0.5 wt % INT–$WS_2$ | 0.27 | 0.23 | 0.43 | 0.35 | 0.31 | 0.09 | 1.29 | 1.03 | 1.26 | 0.43 |

The favorable effect of the nanotubes on the friction is obvious in all cases. Also, in all cases, the wet friction was smaller than under dry conditions (excluding the case of the PLLA 24 blank). Importantly, the polymer coating containing the nanotubes exhibit smaller friction than the SS rod (8 mm), although the coated rod is thicker (on the average 8.1 mm). The nanotubes have the smallest effect on PDLLA, which is amorphous.

### *3.8. Raman Spectroscopy*

The Raman spectrum of PLA, including PLLA, was studied before [69,70]. The Raman spectrum of INT–$WS_2$ has been reported in several studies, see Reference [71]. Raman spectra of PLLA 24 films in three different situations (natural, partially stretched, and fully stretched (close to the fracture)) is displayed in Figure S12. The Raman spectra does not vary upon stretching and hence provides no evidence for any change in the composition and crystallinity of the specimen due to the stretching. The remainder of the results of the Raman spectroscopy of the present PLLA films can be found in the Supplementary Materials.

Figure S13 shows the Raman spectra of the different PLLA 24 samples. Furthermore, Raman mapping of the PLLA 24 with 0.5wt % INT–$WS_2$ before tensile test (see Table 3 sample No. 6) is shown for four peaks: 350 (red—nanotubes), 700 (yellow—dicholoromethane), 820 (blue—monomers of lactic acid), and 923 (green—semicrystalline PLLA) $cm^{-1}$ are displayed in Figure 11. The intensity mapping for nanotubes of $WS_2$ (350 $cm^{-1}$) and for semicrystalline PLLA (973 $cm^{-1}$) showed correlation in the intensity maps for these two components and good compatibility between them. In addition, the intensities of the band lines at 700 and 820 $cm^{-1}$ associated with the presence of residual DCM solvent molecules [72] and monomers of lactic acid [73], were highly correlated. This result could suggest that the presence of solvent molecules residues prevented the completion of the polymerization of the lactic acid monomers.

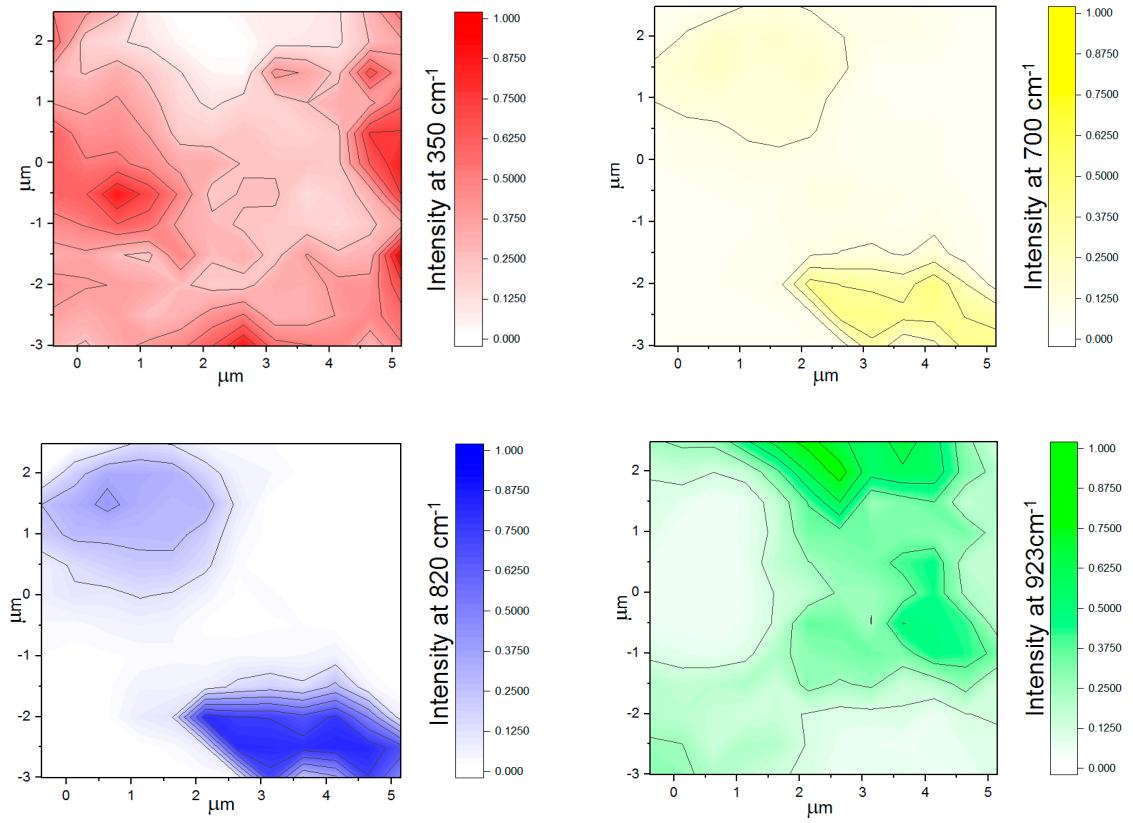


**Figure 11.** Raman intensity mapping of PLLA 24 film with 0.5 wt % before the (natural) tensile test. Intensity mapping at the same area (5 µm × 5 µm) for INT–$WS_2$ (at 350 $cm^{-1}$—red), for DCM (at 700 $cm^{-1}$—yellow), for monomers of lactic acid (at 820 $cm^{-1}$—blue), and for PLLA semicrystalline (at 923 $cm^{-1}$—green).

Raman mapping of the stretched PLLA 24 + INT indicated no monomer residues (not shown) left in the nanocomposite after the failure. The absence of the solvent moieties can be attributed to the weaker signal from the distorted sample, or perhaps to a solvent evaporation resulting from the thermal energy dissipated in the stretching of the specimen.

The reinforcement mechanisms of polymer matrices with nanoparticles fillers have been studied extensively, see for example References [74–77]. Clearly, the dispersion of the nanotubes (nanoparticles) in the polymer matrix is a prime factor. For that to be accomplished, the nanotubes must be deagglomerated in the solvent (for the casting process). Fortunately, the adhesion forces between the $WS_2$ nanotubes are not prohibitive for facile dispersion. Hence, mild combination of mechanical grinding and light ultrasonic treatment, which induce little damage and do not lead to shortening of the $WS_2$ nanotubes, is adequate. Being good lubricants, the nanotubes mix very well in the solvent–polymer blend and, consequently, their mixing does not require a large investment of mechanical shear. Fortunately, this behavior is not limited to the present casting process. The minimal increase in the viscosity often leads to facile blending of the nanotubes in different polymer matrices. The role of the interfacial interaction between the nanotube (nanoparticle) and the polymer matrix has been discussed extensively [74]. Surface modifications were shown to enhance the stress transfer from the polymer matrix to carbon nanotubes, improving thereby the mechanical properties of the nanocomposite [74]. The strength of the multiwall $WS_2$ nanotubes >16 GPa [28] is at least two orders of magnitude larger than the PLLA matrix, and hence, they are not likely to easily break at the failure point. Therefore, a pulling-out mechanism is more likely to occur in this case. The large strain of the nanotubes (>10%) [28,78,79] enables them to extend without failure during the loading, also contributing to the increased elongation (increased fracture toughness) of the nanocomposite. The specific gravity of the nanotubes is rather high (>5 $g/cm^3$). Therefore, the atomic concentration

of the nanotubes is rather low <0.3 at %. However, the long evaporation time of the solvent during casting allowed the nanotubes to precipitate, thereby compromising their uniform distribution in the solidified matrix. Obviously, the nucleation of PLLA crystallites during the solvent evaporation was a prime factor in enhancing the mechanical properties of the polymer matrix. This study, together with the fact that these nanotubes are found to exhibit minor toxicity [34–38], opens up several opportunities to further explore these nanocomposites for different applications.

## 4. Conclusions

In conclusion, the effect of adding different concentrations of $WS_2$ nanotubes on the mechanical properties of biodegradable polymers was studied. The mechanical properties of PLLA with different weight percentage of INT–$WS_2$ showed a large improvement as the weight percent increased to 0.5 wt % but were reduced beyond this concentration. The micro-XCT of PLLA with nanotubes showed clear evidence for the influence of the nanotubes' dispersion on the mechanical properties of the nanocomposite. Two kinds of friction tests were performed with the polymers showing large reduction of the friction of the polymers upon composing them with the nanotubes. Rheological measurements show that, in contrast to other nano-fillers, the nanotubes have no adverse influence on the viscosity and the moduli of the polymer matrix, and this could be an advantage in the manufacturing process of this nanocomposites. Raman analysis shows some changes in the composite of the PLLA matrix due to the addition of the nanotubes and stretching of the nanocomposite. Also, there is no interference with adhesion between the nanotubes and the polymer matrix and the residues of the solvent prevent of the polymer from polymerization. The DSC analysis showed that the nanotubes induce higher crystallinity in the PLLA, likely due to their serving as nucleation center. Raman and XRD measurements confirm that the PLLA is semi-crystalline. However, minor amounts of lactic acid monomer and solvent molecules were found in the polymer matrix. The present results suggest various applications of this nanocomposite, primarily in medical technologies.

**Supplementary Materials:** Supplementary Materials are available online at http://www.mdpi.com/2075-4442/7/3/28/s1.

**Author Contributions:** H.S. Methodology and validation; X.S. validation and formal analysis; O.E. investigation; V.B. methodology and validation; R.R. curation; I.P. formal analysis; Y.F. formal analysis; N.K. formal analysis; H.D.W. supervision; N.L. supervision; R.T. conceptualization and writing.

**Funding:** This research was supported by the KAMIN grant No. 713080 of the Israeli Innovation Authority. We acknowledge the support of the Irving and Cherna Moskowitz Center for Nano and Bio-Nano Imaging; the Perlman Family Foundation; the Kimmel Center for Nanoscale Science Grant No. 43535000350000; and the Irving and Azelle Waltcher Foundations in honor of Prof. M. Levy Grant No. 720821.

**Acknowledgments:** H.D. Wagner would like to acknowledge support from the G.M.J. Schmidt Minerva Centre of Supramolecular Architectures at the Weizmann Institute. H.D. Wagner is the recipient of the Livio Norzi Professorial Chair in Materials Science.

**Conflicts of Interest:** The authors declare no conflict of interest.

## References

1. Saeidlou, S.; Huneault, M.A.; Li, H.; Park, C.B. Poly(lactic acid) crystallization. *Prog. Polym. Sci.* **2012**, *37*, 1657–1677. [CrossRef]
2. Schick, C. Differential scanning calorimetry (DSC) of semicrystalline polymers. *Anal. Bioanal. Chem.* **2009**, *395*, 1589–1611. [CrossRef] [PubMed]
3. Androsch, R.; Zhuravlev, E.; Schick, C. Solid-state reorganization, melting and melt-recrystallization of conformationally disordered crystals (α′-phase) of poly (l-lactic acid). *Polymer (Guildf.)* **2014**, *55*, 4932–4941. [CrossRef]
4. Righetti, M.C.; Gazzano, M.; Di Lorenzo, M.L.; Androsch, R. Enthalpy of melting of α′- and α-crystals of poly(L-lactic acid). *Eur. Polym. J.* **2015**, *70*, 215–220. [CrossRef]
5. Androsch, R.; Di Lorenzo, M.L. Effect of molar mass on the α′/α-transition in poly(L-lactic acid). *Polymer (Guildf.)* **2017**, *114*, 144–148. [CrossRef]

6. Righetti, M.C.; Tombari, E. Crystalline, mobile amorphous and rigid amorphous fractions in poly(L-lactic acid) by TMDSC. *Thermochim. Acta* **2011**, *522*, 118–127. [CrossRef]
7. Brás, A.R.; Viciosa, M.T.; Wang, Y.; Dionísio, M.; Mano, J.F. Crystallization of poly(L-lactic acid) probed with dielectric relaxation spectroscopy. *Macromolecules* **2006**, *39*, 6513–6520. [CrossRef]
8. Van de Velde, K.; Kiekens, P. Biopolymers: Overview of several properties and consequences on their applications. *Polym. Test.* **2002**, *21*, 433–442. [CrossRef]
9. Rezwana, K.; Chena, Q.Z.; Blakera, J.J.; Boccaccini, A.R. Biodegradable and bioactive porous polymer/inorganic composite scaffolds for bone tissue engineering. *Biomaterials* **2006**, *27*, 3413–3431. [CrossRef] [PubMed]
10. Park, S.-D.; Todo, M.; Arakawa, K. Effect of annealing on fracture mechanism of biodegradable poly(lactic acid). *J. Mater. Sci.* **2004**, *39*, 1113–1116. [CrossRef]
11. Moon, S.I.; Jin, F.; Lee, C.J.; Tsutsumi, S.; Hyon, S.H. Novel carbon nanotube/poly(L-lactic acid) nanocomposites; their modulus, thermal stability, and electrical conductivity. *Macromol. Symp.* **2005**, *224*, 287–295. [CrossRef]
12. Klonos, P.; Terzopoulou, Z.; Koutsoumpis, S.; Zidropoulos, S.; Kripotou, S.; Papageorgiou, G.Z.; Bikiaris, D.N.; Kyritsis, A.; Pissis, P. Rigid amorphous fraction and segmental dynamics in nanocomposites based on poly(L–lactic acid) and nano-inclusions of 1–3D geometry studied by thermal and dielectric techniques. *Eur. Polym. J.* **2016**, *82*, 16–34. [CrossRef]
13. Terzopoulou, Z.; Klonos, P.A.; Kyritsis, A.; Tziolas, A.; Avgeropoulos, A.; Papageorgiou, G.Z.; Bikiaris, D.N. Interfacial interactions, crystallization and molecular mobility in nanocomposites of Poly(lactic acid) filled with new hybrid inclusions based on graphene oxide and silica nanoparticles. *Polymer (Guildf.)* **2019**, *166*, 1–12. [CrossRef]
14. Leng, J.; Purohit, P.J.; Kang, N.; Wang, D.-Y.; Falkenhagen, J.; Emmerling, F.; Thünemann, A.F.; Schönhals, A. Structure–property relationships of nanocomposites based on polylactide and MgAl layered double hydroxides. *Eur. Polym. J.* **2015**, *68*, 338–354. [CrossRef]
15. Saiter, A.; Delpouve, N.; Dargent, E.; Oberhauser, W.; Conzatti, L.; Cicogna, F.; Passaglia, E. Probing the chain segment mobility at the interface of semi-crystalline polylactide/clay nanocomposites. *Eur. Polym. J.* **2016**, *78*, 274–289. [CrossRef]
16. Pluta, M.; Jeszka, J.K.; Boiteux, G. Polylactide/montmorillonite nanocomposites: Structure, dielectric, viscoelastic and thermal properties. *Eur. Polym. J.* **2007**, *43*, 2819–2835. [CrossRef]
17. Purohit, P.J.; Wang, D.-Y.; Wurm, A.; Schick, C.; Schönhals, A. Comparison of thermal and dielectric spectroscopy for nanocomposites based on polypropylene and Layered Double Hydroxide—Proof of interfaces. *Eur. Polym. J.* **2014**, *55*, 48–56. [CrossRef]
18. Kuan, C.F.; Chen, C.H.; Kuan, H.C.; Lin, K.C.; Chiang, C.L.; Peng, H.C. Multi-walled carbon nanotube reinforced poly(L-lactic acid) nanocomposites enhanced by water-crosslinking reaction. *J. Phys. Chem. Solids* **2008**, *69*, 1399–1402. [CrossRef]
19. Leal, C.V.; Martinez, D.S.T.; Más, B.A.; Alves, O.L.; Duek, E.A.R. Influence of purified multiwalled carbon nanotubes on the mechanical and morphological behavior in poly (L-lactic acid) matrix. *J. Mech. Behav. Biomed. Mater.* **2016**, *59*, 547–560. [CrossRef]
20. Obarzanek-Fojt, M.; Elbs-Glatz, Y.; Lizundia, E.; Diener, L.; Sarasua, J.-R.; Bruinink, A. From implantation to degradation—Are poly (L-lactide)/multiwall carbon nanotube composite materials really cytocompatible? *Nanomed. Nanotechnol. Biol. Med.* **2014**, *10*, 1041–1051. [CrossRef] [PubMed]
21. Ko, S.W.; Gupta, R.K.; Bhattacharya, S.N.; Choi, H.J. Rheology and physical characteristics of synthetic biodegradable aliphatic polymer blends dispersed with MWNTs. *Macromol. Mater. Eng.* **2010**, *295*, 320–328. [CrossRef]
22. Ivanova, R.; Kotsilkova, R. Rheological study of poly(lactic) acid nanocomposites with carbon nanotubes and graphene additives as a tool for materials characterization for 3D printing application. *Appl. Rheol.* **2018**, *28*, 54014–54023.
23. Jonoobi, M.; Harun, J.; Mathew, A.P.; Oksman, K. Mechanical properties of cellulose nanofiber (CNF) reinforced polylactic acid (PLA) prepared by twin screw extrusion. *Compos. Sci. Technol.* **2010**, *70*, 1742–1747. [CrossRef]

24. Huda, M.S.; Drzal, L.T.; Mohanty, A.K.; Misra, M. Chopped glass and recycled newspaper as reinforcement fibers in injection molded poly(lactic acid) (PLA) composites: A comparative study. *Compos. Sci. Technol.* **2006**, *66*, 1813–1824. [CrossRef]
25. Luo, Y.-B.; Li, W.-D.; Wang, X.-L.; Xu, D.-Y.; Wang, Y.-Z. Preparation and properties of nanocomposites based on poly(lactic acid) and functionalized $TiO_2$. *Acta Mater.* **2009**, *57*, 3182–3191. [CrossRef]
26. Foruzanmehr, M.; Vuillaume, P.Y.; Elkoun, S.; Robert, M. Physical and mechanical properties of PLA composites reinforced by $TiO_2$ grafted flax fibers. *Mater. Des.* **2016**, *106*, 295–304. [CrossRef]
27. Tenne, R. Advances in the synthesis of inorganic nanotubes and fullerene-like nanoparticles. *Angew. Chem. Int. Ed.* **2003**, *42*, 5124–5132. [CrossRef]
28. Kaplan-Ashiri, I.; Cohen, S.R.; Gartsman, K.; Ivanovskaya, V.; Heine, T.; Seifert, G.; Wiesel, I.; Wagner, H.D.; Tenne, R. On the mechanical behavior of $WS_2$ nanotubes under axial tension and compression. *Proc. Natl. Acad. Sci. USA* **2006**, *103*, 523–528. [CrossRef]
29. Rozenberg, B.A.; Tenne, R. Polymer-assisted fabrication of nanoparticles and nanocomposites. *Prog. Polym. Sci.* **2008**, *33*, 40–112. [CrossRef]
30. Sedova, A.; Bar, G.; Goldbart, O.; Ron, R.; Achrai, B.; Kaplan-Ashiri, I.; Brumfeld, V.; Zak, A.; Gvishi, R.; Wagner, H.D.; et al. Reinforcing silica aerogels with tungsten disulfide nanotubes. *J. Supercrit. Fluids* **2015**, *106*, 9–15. [CrossRef]
31. Sonker, A.K.; Wagner, H.D.; Bajpai, R.; Tenne, R.; Sui, X. Effects of tungsten disulphide nanotubes and glutaric acid on the thermal and mechanical properties of polyvinyl alcohol. *Compos. Sci. Technol.* **2016**, *127*, 47–53. [CrossRef]
32. Goldbart, O.; Sedova, A.; Yadgarov, L.; Rosentsveig, R.; Shumalinsky, D.; Lobik, L.; Wagner, H.D.; Tenne, R. Lubricating medical devices with fullerene-like nanoparticles. *Tribol. Lett.* **2014**, *55*, 103–109. [CrossRef]
33. Goldbart, O.; Elianov, O.; Shumalinsky, D.; Lobik, L.; Cytron, S.; Rosentsveig, R.; Wagner, H.D.; Tenne, R. Study of urological devices coated with fullerene-like nanoparticles. *Nanoscale* **2013**, *5*, 8526–8532. [CrossRef]
34. Shneider, M.; Rapoport, L.; Moshkovich, A.; Dodiuk, H.; Kenig, S.; Tenne, R.; Zak, A. Tribological performance of the epoxy-based composite reinforced by $WS_2$ fullerene-like nanoparticles and nanotubes. *Phys. Status Solidi* **2013**, *210*, 2298–2306. [CrossRef]
35. Ke, S.; Lai, Y.; Zhou, T.; Li, L.; Wang, Y.; Ren, L.; Ye, S. Molybdenum disulfide nanoparticles resist oxidative stress-mediated impairment of autophagic flux and mitigate endothelial cell senescence and angiogenic dysfunctions. *ACS Biomater. Sci. Eng.* **2018**, *4*, 663–674. [CrossRef]
36. Wu, X.; Tian, X.; Chen, T.; Zeng, A.; Yang, G. Inorganic fullerene-like molybdenum selenide with good biocompatibility synthesized by laser ablation in liquids. *Nanotechnology* **2018**, *29*, 295604. [CrossRef] [PubMed]
37. Fojtů, M.; Teo, W.Z.; Pumera, M. Environmental impact and potential health risks of 2D nanomaterials. *Environ. Sci. Nano* **2017**, *4*, 1617–1633. [CrossRef]
38. Pardo, M.; Shuster-Meiseles, T.; Levin-Zaidman, S.; Rudich, A.; Rudich, Y. Low cytotoxicity of inorganic nanotubes and fullerene-like nanostructures in human bronchial epithelial cells: Relation to inflammatory gene induction and antioxidant response. *Environ. Sci. Technol.* **2014**, *48*, 3457–3466. [CrossRef] [PubMed]
39. Pham, V.H.; Cuong, T.V.; Hur, S.H.; Oh, E.; Kim, E.J.; Shin, E.W.; Chung, J.S. Chemical functionalization of graphene sheets by solvothermal reduction of a graphene oxide suspension in N-methyl-2-pyrrolidone. *J. Mater. Chem.* **2011**, *21*, 3371–3377. [CrossRef]
40. Hernandez, Y.; Nicolosi, V.; Lotya, M.; Blighe, F.M.; Sun, Z.; De, S.; McGovern, I.T.; Holland, B.; Byrne, M.; Gun'ko, Y.K.; et al. High-yield production of graphene by liquid-phase exfoliation of graphite. *Nat. Nanotechnol.* **2008**, *3*, 563–568. [CrossRef] [PubMed]
41. Choi, E.Y.; Han, T.H.; Hong, J.; Kim, J.E.; Lee, S.H.; Kim, H.W.; Kim, S.O. Noncovalent functionalization of graphene with end-functional polymers. *J. Mater. Chem.* **2010**, *20*, 1907–1912. [CrossRef]
42. Giordani, S.; Bergin, S.D.; Nicolosi, V.; Lebedkin, S.; Kappes, M.M.; Blau, W.J.; Coleman, J.N. Debundling of single-walled nanotubes by dilution: Observation of large populations of individual nanotubes in amide solvent dispersions. *J. Phys. Chem. B* **2006**, *110*, 15708–15718. [CrossRef] [PubMed]
43. Furtado, C.A.; Kim, U.J.; Gutierrez, H.R.; Pan, L.; Dickey, E.C.; Peter, C. Eklund Debundling and dissolution of single-walled carbon nanotubes in amide solvents. *J. Am. Chem. Soc.* **2004**, *126*, 6095–6105. [CrossRef] [PubMed]

44. Sahu, M.; Narashimhan, L.; Prakash, O.; Raichur, A.M. Noncovalently functionalized tungsten disulfide nanosheets for enhanced mechanical and thermal properties of epoxy nanocomposites. *ACS Appl. Mater. Interfaces* **2017**, *9*, 14347–14357. [CrossRef]
45. Kim, I.S.; Lee, S.K.; Park, Y.M.; Lee, Y.B.; Shin, S.C.; Lee, K.C.; Oh, I.J. Physicochemical characterization of poly(L-lactic acid) and poly(D,L-lactide-co-glycolide) nanoparticles with polyethylenimine as gene delivery carrier. *Int. J. Pharm.* **2005**, *298*, 255–262. [CrossRef]
46. Zhao, H.; Li, Y.; Tan, B.; Zhang, Y.; Chen, X.; Quan, X. PEGylated molybdenum dichalcogenide (PEG-$MoS_2$) nanosheets with enhanced peroxidase-like activity for the colorimetric detection of $H_2O_2$. *New J. Chem.* **2017**, *41*, 6700–6708. [CrossRef]
47. Sacchetti, C.; Motamedchaboki, K.; Magrini, A.; Palmieri, G.; Mattei, M.; Bernardini, S.; Rosato, N.; Bottini, N.; Bottini, M. Surface polyethylene glycol conformation influences the protein corona of polyethylene glycol-modified single-walled carbon nanotubes: Potential implications on biological performance. *ACS Nano* **2013**, *7*, 1974–1989. [CrossRef] [PubMed]
48. Díez-Pascual, A.M.; Díez-Vicente, A.L. Poly(propylene fumarate)/polyethylene glycol-modified graphene oxide nanocomposites for tissue engineering. *ACS Appl. Mater. Interfaces* **2016**, *8*, 17902–17914. [CrossRef]
49. Huang, W.; Fernando, S.; Allard, L.F.; Sun, Y.P. Solubilization of single-walled carbon nanotubes with diamine-terminated oligomeric poly(ethylene glycol) in different functionalization reactions. *Nano Lett.* **2003**, *3*, 565–568. [CrossRef]
50. Landi, B.J.; Ruf, H.J.; Worman, J.J.; Raffaelle, R.P. Effects of alkyl amide solvents on the dispersion of single-wall carbon nanotubes. *J. Phys. Chem. B* **2004**, *108*, 17089–17095. [CrossRef]
51. Naffakh, M.; Marco, C.; Ellis, G. Development of novel melt-processable biopolymer nanocomposites based on poly(L-lactic acid) and $WS_2$ inorganic nanotubes. *CrystEngComm* **2014**, *16*, 5062–5072. [CrossRef]
52. Naffakh, M.; Marco, C.; Ellis, G. Inorganic $WS_2$ nanotubes that improve the crystallization behavior of poly(3-hydroxybutyrate). *CrystEngComm* **2014**, *16*, 1126–1135. [CrossRef]
53. Silverman, T.; Naffakh, M.; Marco, C.; Ellis, G.; Silverman, T.; Naffakh, M.; Marco, C.; Ellis, G. Effect of $WS_2$ inorganic nanotubes on isothermal crystallization behavior and kinetics of poly(3-hydroxybutyrate-co-3-hydroxyvalerate). *Polymers (Basel)* **2018**, *10*, 166. [CrossRef]
54. Rapoport, L.; Fleischer, N.; Tenne, R. Applications of $WS_2$($MoS_2$) inorganic nanotubes and fullerene-like nanoparticles for solid lubrication and for structural nanocomposites. *J. Mater. Chem.* **2005**, *15*, 1782–1788. [CrossRef]
55. Rosentsveig, R.; Gorodnev, A.; Feuerstein, N.; Friedman, H.; Zak, A.; Fleischer, N.; Tannous, J.; Dassenoy, F.; Tenne, R. Fullerene-like $MoS_2$ nanoparticles and their tribological behavior. *Tribol. Lett.* **2009**, *36*, 175–182. [CrossRef]
56. Samorodnitzky-Naveh, G.R.; Redlich, M.; Rapoport, L.; Feldman, Y.; Tenne, R. Inorganic fullerene-like tungsten disulfide nanocoating for friction reduction of nickel–titanium alloys. *Nanomedicine* **2009**, *4*, 943–950. [CrossRef] [PubMed]
57. Goldbart, O.; Cohen, S.R.; Kaplan-Ashiri, I.; Glazyrina, P.; Wagner, H.D.; Enyashin, A.; Tenne, R. Diameter-dependent wetting of tungsten disulfide nanotubes. *Proc. Natl. Acad. Sci. USA* **2016**, *113*, 13624–13629. [CrossRef]
58. Israelachvili, J.; Drummond, C.; Golan, Y.; Tenne, R.; Alcantar, N. Microtribology and friction-induced material transfer in $WS_2$ nanoparticle additives. *Adv. Funct. Mater.* **2001**, *11*, 348–354.
59. Maharaj, D.; Bhushan, B. Effect of $MoS_2$ and $WS_2$ nanotubes on nanofriction and wear reduction in dry and liquid environments. *Tribol. Lett.* **2013**, *49*, 323–339. [CrossRef]
60. Yadgarov, L.; Petrone, V.; Rosentsveig, R.; Feldman, Y.; Tenne, R.; Senatore, A. Tribological studies of rhenium doped fullerene-like $MoS_2$ nanoparticles in boundary, mixed and elasto-hydrodynamic lubrication conditions. *Wear* **2013**, *297*, 1103–1110. [CrossRef]
61. Zak, A.; Sallacan-Ecker, L.; Margolin, A.; Feldman, Y.; Popovitz-Biro, R.; Albu-Yaron, A.; Genut, M.; Tenne, R. Scaling up of the $WS_2$ nanotubes synthesis. *Fuller. Nanotubes Carbon Nanostruct.* **2011**, *19*, 18–26. [CrossRef]
62. Steffe, J.F. *Rheological Methods in Food Process Engineering*; Freeman Press: East Lansing, MI, USA, 1996.
63. Mata, D.; Horovistiz, A.L.; Branco, I.; Ferro, M.; Ferreira, N.M.; Belmonte, M.; Lopes, M.A.; Silva, R.F.; Oliveira, F.J. Carbon nanotube-based bioceramic grafts for electrotherapy of bone. *Mater. Sci. Eng. C* **2014**, *34*, 360–368. [CrossRef] [PubMed]

64. Androsch, R.; Iqbal, H.M.M.N.; Schick, C. Non-isothermal crystal nucleation of poly(L-lactic acid). *Polymer (Guildf.)* **2015**, *81*, 151–158. [CrossRef]
65. Shenoy, A.V. *Rheology of Filled Polymer Systems*; Springer: Berlin, Germany, 1999.
66. Pötschke, P.; Fornes, T.D.; Paul, D.R. Rheological behavior of multiwalled carbon nanotube/polycarbonate composites. *Polymer (Guildf.)* **2002**, *43*, 3247–3255. [CrossRef]
67. Song, Y.S.; Youn, J.R. Influence of dispersion states of carbon nanotubes on physical properties of epoxy nanocomposites. *Carbon N. Y.* **2005**, *43*, 1378–1385. [CrossRef]
68. Rapoport, L.; Bilik, Y.; Feldman, Y.; Homyonfer, M.; Cohen, S.R.; Tenne, R. Hollow nanoparticles of $WS_2$ as potential solid-state lubricants. *Nature* **1997**, *387*, 791–793. [CrossRef]
69. Kister, G.; Cassanas, G.; Vert, M.; Pauvert, B.; Térol, A. Vibrational analysis of poly(L-lactic acid). *J. Raman Spectrosc.* **1995**, *26*, 307–311. [CrossRef]
70. Kister, G.; Cassanas, G.; Vert, M. Effects of morphology, conformation and configuration on the IR and Raman spectra of various poly(lactic acid)s. *Polymer (Guildf.)* **1998**, *39*, 267–273. [CrossRef]
71. Grinberg, O.; Deng, S.; Zussman, E.; Livneh, T.; Zak, A. Raman scattering from single $WS_2$ nanotubes in stretched PVDF electrospun fibers. *Phys. Chem. Chem. Phys.* **2017**, *19*, 18443–18451. [CrossRef]
72. Chen, S.J.H.; Schwartz, M. Raman study of vibrational relaxation in dichloromethane and [2H2]dichloromethane. *J. Chem. Soc. Faraday Trans. 2 Mol. Chem. Phys.* **1985**, *81*, 235–243. [CrossRef]
73. Cassanas, G.; Morssli, M.; Fabrègue, E.; Bardet, L. Vibrational spectra of lactic acid and lactates. *J. Raman Spectrosc.* **1991**, *22*, 409–413. [CrossRef]
74. Eitan, A.; Fisher, F.T.; Andrews, R.; Brinson, L.C.; Schadler, L.S. Reinforcement mechanisms in MWCNT-filled polycarbonate. *Compos. Sci. Technol.* **2006**, *66*, 1162–1173. [CrossRef]
75. Gersappe, D. Molecular Mechanisms of Failure in Polymer Nanocomposites. *Phys. Rev. Lett.* **2002**, *89*, 058301. [CrossRef]
76. Dorigato, A.; Dzenis, Y.; Pegoretti, A. Filler aggregation as a reinforcement mechanism in polymer nanocomposites. *Mech. Mater.* **2013**, *61*, 79–90. [CrossRef]
77. Wagner, H.D.; Vaia, R.A. Nanocomposites: Issues at the interface. *Mater. Today* **2004**, *7*, 38–42. [CrossRef]
78. Lorenz, T.; Teich, D.; Joswig, J.O.; Seifert, G. Theoretical study of the mechanical behavior of individual $TiS_2$ and $MoS_2$ nanotubes. *J. Phys. Chem. C* **2012**, *116*, 11714–11721. [CrossRef]
79. Zibouche, N.; Ghorbani-Asl, M.; Heine, T.; Kuc, A. Electromechanical Properties of Small Transition-Metal Dichalcogenide Nanotubes. *Inorganics* **2014**, *2*, 155–167. [CrossRef]